Chemistry*OPEN*

Including Thesis Treasury

Reprint

WILEY-VCH

A Journal of

ChemPubSoc Europe

# Electrospun Carbon/Cu$_x$O Nanocomposite material as Sustainable and High Performance Anode for Lithium-Ion Batteries

Fabio Maroni,[a] Pantaleone Bruni,[a] Gabriele Giuli,[b] S. Brutti,[c] and Fausto Croce*[a]

The increase in energy density of the next generation of battery materials to meet the new challenges of the electrical vehicles era calls for innovative and easily scalable materials with sustainable processes. An innovative Cu$_x$O/C nanocomposite material, characterized by a highly conductive 3D-framework, with Cu$_x$O/Cu-metal contiguous nanodomains is prepared by electrospinning. The electrode processing is made using a polyacrylic acid binder. The nanocomposite has been fully characterized and the electrochemical performance shows high specific capacity values over 450 galvanostatic cycles at 500 mAg^{-1} specific current with capacity retention values over 80%. In addition, the composite shows remarkable high rate performance and highly stable interface, which has been studied by impedance spectroscopy.

Introduction

Lithium ion batteries (LIBs) are currently the most performing and widespread electrochemical energy storage system to provide power to portable electronic devices such as smartphones and laptops. The ongoing increase in the electrical vehicles (EVs) market is leading for breakthrough in cell energy density.[1] The traditional graphite-based anodes possess a theoretical specific capacity of 372 mAhg^{-1} thus the investigation and development of higher theoretical capacity anode materials with low operating voltage vs. Li$^+$/Li couple is needed to fulfill these objectives. This increase in energy density could be achieved by exploiting different lithium storage chemistries such as alloying and conversion mechanisms.[2,3] Conversion reaction has been subject of intensive research in these last few years and several materials surfaced as possible anode candidates. A general reaction resuming the conversion mechanism is reported in equation 1:

$$M_xO_y + 2ye^- + 2yLi^+ \leftrightarrow xM^0 + yLi_2O \tag{1}$$
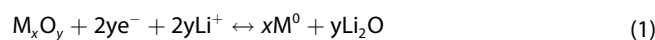
Among the conversion enabled chemical compounds can be found transition metal oxides (TMOs),[4–7] nitrides,[8] sulfides[9] and fluorides.[10] TMOs have the advantage to be fairly easy to be found, they are cheap and possess high theoretical specific capacities. During a conversion reaction cycle, TMOs particles are reversibly reduced to metal nanoparticles embedded in a Li$_2$O matrix and vice versa. Despite the good premises, the conversion mechanism presents several drawbacks such as volume expansion, relatively high working potential vs Li$^+$/Li^0 couple, high potential hysteresis and low electronic conductivity of the TMOs candidates. To overcome these issues, several strategies have been employed, mainly reducing particle size,[11,12] the use of innovative morphologies,[13–15] the implementation of carbon matrices[16–19] and recently, the use of graphene.[20–23] Between them, the adoption of effective carbon supporting matrices is not always easy, and often requires the adoption of complex syntheses and techniques which hamper their scale up on an industrial perspective. To easily obtain innovative morphologies while implementing effective 3-D support and conducting frameworks, electrospinning has gained much attention due to its relatively easy experimental setup, operational straightforwardness and scale up capabilities.[24–29] In addition to that, also electrode processing of the final composite material has a determining impact on sustainability and cycling performance.[30–33] In this work we present the easy and scalable electrospinning synthesis procedure of a Cu$_2$O/PAN derived carbon nanocomposite, coupled with an improved and sustainable electrode processing procedure based on the PolyAcrylic Acid (PAA)-Ethanol binder/solvent couple which ensured high performance on a long cycling life perspective.

[a] Dr. F. Maroni, Dr. P. Bruni, Prof. F. Croce
 Dipartimento di Farmacia
 Università Degli Studi di Chieti-Pescara "G. D'Annunzio"
 Via Dei Vestini, 31
 66100-Chieti
 E-mail: Fausto.croce@unich.it
[b] Prof. G. Giuli
 Dipartimento di Scienze della Terra
 Università Degli Studi Di Camerino
 Via Gentile III da Varano, 27
 62032-Camerino (MC)
[c] S. Brutti
 Dipartimento di Chimica
 Università di Roma "La Sapienza"
 Piazzale Aldo Moro, 3
 00185-Roma
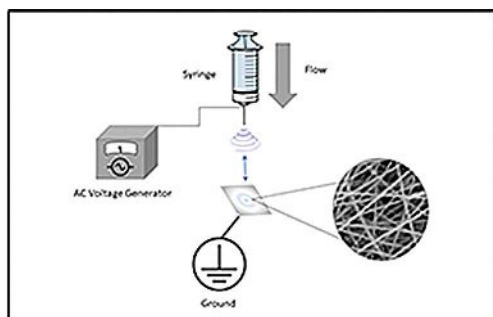
Figure 1. Electrospinning apparatus schematics.

Figure 2. Nanocomposite characterization-XRD pattern.

Results and Discussion

The Cu_2O–C nanocomposite was prepared by means of an electrospinning methodology. This technique, has a wide literature coverage about synthesis of materials with a fibrous morphology, has a fairly easy experimental setup, as shown Figure 1, and allows to tune a wide number of parameters which enable a remarkable flexibility in terms of operating conditions, resulting in a great variety of morphologies.[34–36] In this work, the polymer precursor of choice has been PolyAcrylonitrile, dissolved in DMF solvent. Then, CuO nanoparticles were added to the blend and nanofiber mats were obtained, using optimized conditions, improved during the development of the work. At this point, the thermal processing of the precursor material is a crucial step in order to obtain an effective and highly conductive carbon matrix, while maintaining a consistent morphology at the end of the synthesis. The first thermal step has been an oxidative stabilization in air atmosphere,[37] at 250 °C in which Polyacrylonitrile undergoes a complex series of intramolecular cyclization of the nitrile (–C≡N) groups, a dehydrogenation, and oxidation step which leads to intermolecular cross-linking of the polymer chains. At this stage, CuO particles are not affected by the oxidative conditions since, copper is already in the +2 oxidation state. The final thermal annealing step, carried out in $Ar:H_2$ 95:5 atmosphere at 700 °C, enables the sp^2 conducting network of the PAN-derived fibers, and reduces the CuO particles to copper metal and copper (I) oxide nanoparticles, enabling a contiguous structure between nanocrystalline domain which is favorable for electrochemical performance.

The XRD pattern, reported in Figure 2, was recorded by means of a long acquisition time, in order to have a better resolution and to identify all the crystalline phases present in the nanocomposite. Diffractometric data shows a quite large peak between 26° and 30° due to the amorphous carbon matrix, a low intensity peak at 36.22°, which was assigned to Cu_2O (JCPDS Card N. 05-667) and finally two sharp and intense peaks, assigned to copper metal (JCPDS Card N.04-0836) at 40.26° and 50.33°, respectively. In Figure S1a, thermogravimetric analysis, carried out in air atmosphere between 30 °C and 950 °C at 10 °Cmin^{-1} heating ramp, shows a first weight loss of 5.36% up to 178 °C likely due to moisture and adsorbed volatile species, then a gradual weight increase up to 297 °C, which was
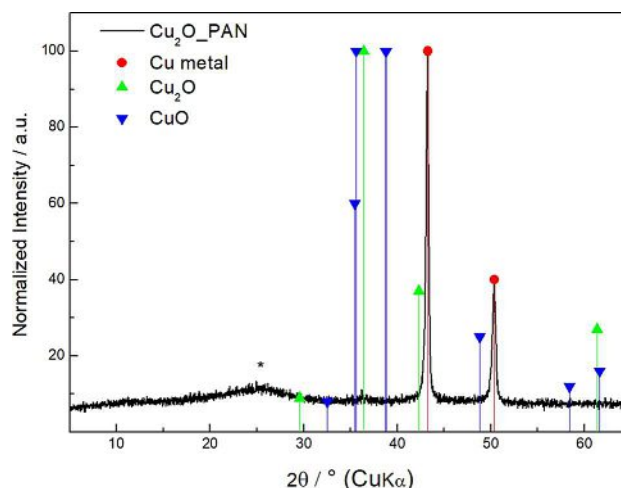
assigned to the oxidation of Cu_2O nanoparticles to CuO. In the temperature range 300 °C–500 °C, a 59.08% weight loss is evidenced, and was assigned to the parallel conversion of the carbon matrix to CO_2 and the oxidation of copper metal to CuO. The DTG graph, present as dashed line in Figure S1a, evidences a complex process, as well.

Raman spectrum, showed in Figure S1b, shows the typical D and G bands of carbon materials at 1341 cm^{-1} and 1579 cm^{-1} respectively, related to turbostratic disordered structures (D-band) and vibrations of more ordered crystalline nanostructures (G-band).[38,39] The ratio of these two bands can provide an estimation of the degree of order of these carbon structures, the lower the ratio, the more crystalline is the material. In this case, the R = (I_D/I_G) ratio value has been estimated in 0.9, indicating a somewhat short-range ordered carbon structure.[40]

Morphological characterization was done by recording SEM and HR-TEM micrographs. Figure S2a,b report the morphology of the as-prepared electrospun mats, in which sub-micrometer sized fibers are homogenously distributed, with sporadic presence of larger polymer aggregates. Then, in Figure S2c,d, the fiber mats, stabilized at 250 °C in air atmosphere, show a good retention of the of the original morphology, in which part of the agglomerates disappears, due to partial polyacrylonitrile decomposition, as reported previously. Thus, in Figure 3 a,b are shown the $Ar:H_2$ annealed nanocomposite micrographs recorded at different magnification levels, revealing, once more, a quite uniform morphology of the carbon nanofibers, with dimensions of 300 nm–400 nm in width and up to micrometer-sized length. In particular, visible bulges in Figure 3b, highlight the presence of the Cu_xO/Cu particles inside the carbon fibers, as expected. In Figure 3c is reported a micrograph of the mechanically ground powder, before electrode processing, showing a shortened but still fibrous morphology. In the end in Figure 3d, Cu metal and Cu(I) Oxide dispersion has been evaluated using the Backscattered Electrons (BSE) detector of the SEM instrument, which is showed in Figure 3d. To give an additional insight on elemental distribution on the examined samples, in Figure S3, S4 and S5 are reported the EDX maps of
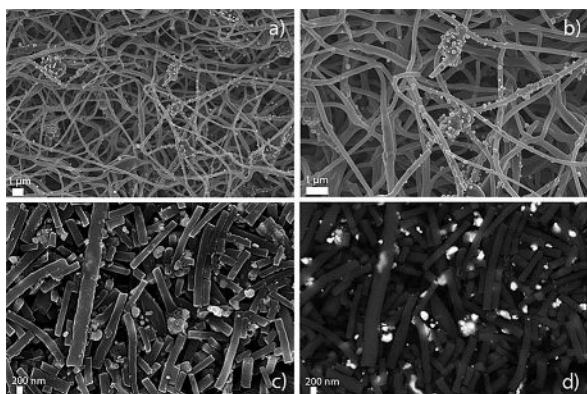
Figure 3. SEM micrographs recorded at a) 10KX; b) 20 KX c) 25 KX d) 25 KX Backscattered Electrons (BSE) image.

the samples at the different preparation stages: pristine, Air-stabilized and Ar:H₂ respectively.

Transition Metal Oxide (TMO) nanoparticles are widely distributed around and inside the carbon nanofibers. This morphology is confirmed by HRTEM analysis, shown in Figure 4. In particular it is possible to observe the elongated micrometric morphology of the carbonaceous matrix derived from the pyrolysis of the pristine polymer precursor (Figure 4a). The diameters of the carbonaceous wires are in the 300–500 nm range, in agreement with the SEM analysis. Besides these elongated morphologies, nano-sized precipitates can be found both over the outer surface and embedded within the carbon matrix, as shown in Figure 4b. These particles are approximately 20–100 nm long in pseudo-diameter and can be either isolated or grouped together. From the structural point of view, few crystalline domains are confined within the same nanoparticle:
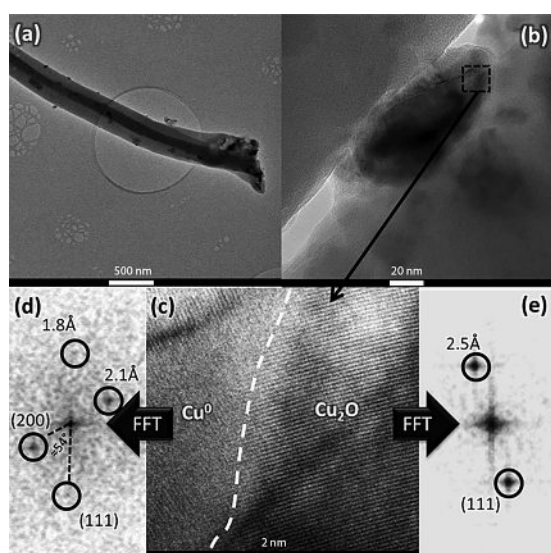
Figure 4. TEM micrographs and selected area FFT analyses. (a) Low Magnification; (b) high magnification, (c) high resolution TEM micrograph of the area identified in the (b) Figure. The dashed white line in the Figure (c) highlights the phase boundary between two crystallites corresponding to the (d) and (e) simulated electron diffraction patterns (FFT reconstructed).

highly crystalline nano-domains can be easily found as well as very well defined phase boundaries, as shown in the bright field high resolution TEM in Figure 4c. The electron beam diffraction patterns of these nano-domains have been reconstructed by FFT and are shown in the Figures 4d and 4e. The observed dark spots can be easily indexed to the diffraction reflections originated by the Cu₂O cP6[41] and the Cu metallic cF4[42] lattices, respectively, in line with the observation of the powder XRD experiments (see Figure 2 above). As a final point it is important to underline that the outer surface of these nanoparticles show an amorphous and rough layer 2–5 nm thick: this morphology is likely due to the presence of a thin carbonaceous film.

In Figure 5, Cyclic Voltammetry carried out at 0.050 mV⁻¹ scan rate, in the potential range 0.005 V–3.000 V, shows peaks relative to the electrochemical activity of the Cu$_x$O/C nano-composite: during the first discharge cycle, peak **A** at potential E = 0.790 V, can be related to both the formation of the SEI layer, due to the decomposition products of the electrolyte salt and solvent mixture,[43–45] and the first conversion of Cu₂O active material to metallic Cu embedded in a Li₂O matrix, following the reaction:

$$Cu_2O + 2Li^+ + 2e^- \quad 2Cu^0 + Li_2O \qquad (2)$$
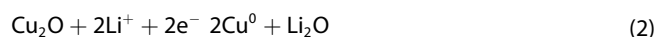
Following up the experiment, peak **B** at E = 0.005 V, evidences Li⁺ ions insertion inside the carbonaceous matrix. In the anodic region of the first cycle, peak **C** at E = 1.260 V has been assigned to Li⁺ ions extraction from carbon structures, and peak **D** at E = 2.400 V has been assigned to the dissolution of the Li₂O matrix and the reversible conversion of Cu to Cu$_x$O.

Cu₂O and CuO electrochemical features are often found to be overlapped in voltammetry tests reported in literature. To shed doubts about the electrochemical mechanism of the active material species in this nanocomposite material, successive voltammetric scans show two weak highly reversible peaks, labeled as **E**, at E = 1.340 V and **F**, at E = 0.860 V, respectively, which have been assigned to a two-step CuO reduction to metallic Cu and Li₂O, consistent with literature data .[14,46,47] Finally, in the anodic region, peak **C** shifts to slightly higher
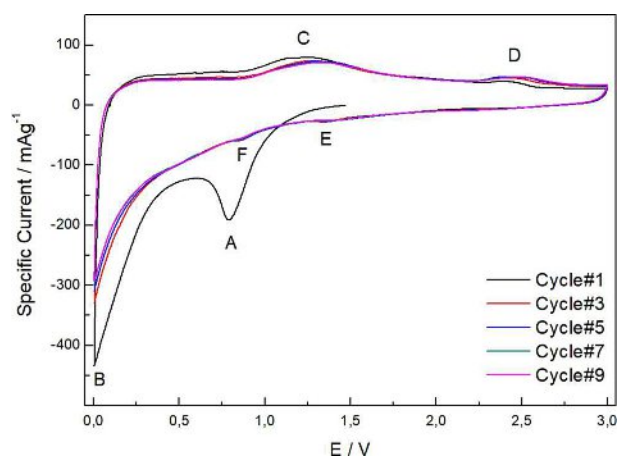

Figure 5. Nanocomposite Cyclic Voltammetry; Potential range 0.005 < E (V) < 3.000; Scan rate υ = 0.050 mV⁻¹

potentials, and peak **D**, increases its intensity and becomes broadened, sign of a progressively increased electrochemical activity. Reversibility remains very good.

The galvanostatic cycling experiment, carried out at $I_{spec} = 500$ mAg^{-1} specific current for 450 cycles, shows the remarkable stability and electrochemical reversibility of the Cu$_2$O/C material.

In Figure 6a, galvanostatic cycling shows a first discharge capacity of 1223 mAhg^{-1} with a coulombic efficiency of 58%, a low value due to the first cycles irreversible processes, like SEI formation, the first electrochemical conversion and the progressive activation of the composite material. In successive cycles coulombic efficiency increases to over 99% during all the experiment. Capacity retention at the end of the experiment is 72.24%. Specific capacity values in the range of 550 mAhg^{-1}–600 mAhg^{-1} remain stable throughout the experiment.
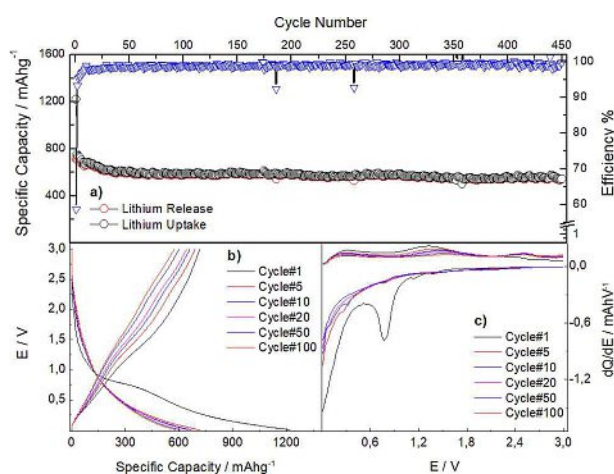

Figure 6. Electrochemical Characterization: galvanostatic Cycling test at 500 mAg^{-1} specific current; Potential range $0.005 < E (V) < 3.000$ V

In Figure 6b, the specific capacity profile of the first discharge cycle, show a sloping plateau at $E = 0.890$ V–$E = 0.800$ V due to the passivation layer formation and the conversion of Cu$_2$O to metallic Cu and Li$_2$O, and successively a sloping line up to the lower cut-off potential due to Li$^+$ insertion processes inside the carbon matrix.[48] Then in the first charge step, two large sloping plateaus are visible, at $E = 1.110$ V and $E = 2.500$ V, which are due to the extraction of the Li$^+$-ions from disordered carbons[49] and to the dissolution of Li$_2$O and the oxidation of Cu to Cu$_x$O, respectively. Successive cycles show featureless profiles during the discharge step, and reversible electrochemical features during the oxidation step.

Differential analysis shown in Figure 6c, in addition to the already evidenced electrochemical processes, consistent with the voltammetric scans, highlights a Li$^+$ ions extraction process at $E = 0.150$ V, in addition to the broad peak at $E = 1.500$ V, consistent with the presence of different carbon structures with different sites and insertion/extraction energies.[39,50]

A rate capability experiment, showed in Figure 7, carried out at specific currents ranging from $I_{spec} = 100$ mAg^{-1} and
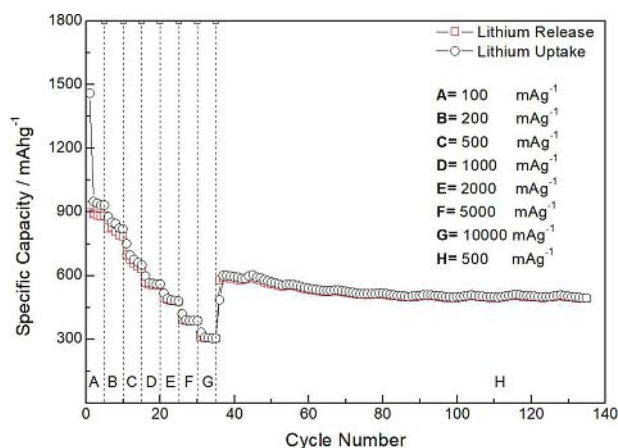
Figure 7. Rate capability experiment at selected specific currents: A = 100 mAg^{-1} - B = 200 mAg^{-1} - C = 500 mAg^{-1} - D = 1000 mAg^{-1} - E = 2000 mAg^{-1} - F = 5000 mAg^{-1} - G = 10000 mAg^{-1} - H = 500 mAg^{-1}

$I_{spec} = 1000$ mAg^{-1}, with 5 galvanostatic cycles at each specific current, shows very good capacity values of 939 mAhg^{-1} at $I_{spec} = 100$ mAg^{-1}, 846 mAhg^{-1} at $I_{spec} = 200$ mAg^{-1}, 675 mAhg^{-1} at $I_{spec} = 500$ mAg^{-1}, 561 mAhg^{-1} at $I_{spec} = 1000$ mAg^{-1}, 485 mAhg^{-1} at $I_{spec} = 2000$ mAg^{-1}, 388 mAhg^{-1} at $I_{spec} = 5000$ mAg^{-1} and 305 mAhg^{-1} a $I_{spec} = 10000$ mAg^{-1}. For the sake of clarity, specific capacity values are resumed in Table S1.

Then, a recovery galvanostatic cycling test has been conducted at Ispec = 500 mAg^{-1}, for 100 cycles. Specific capacity values ranged from 560 mAhg^{-1} to 494 mAhg^{-1}, with a final capacity retention of 82.33%. In this view, the hollow carbon fibers obtained by the electrospinning synthesis, which allowed the containment of the Cu/Cu$_x$O nanoparticles volume variations associated with electrochemical conversion mechanism, are intimately connected with the metallic Cu nanodomains already evidenced by TEM imaging. This enables a highly 3D-conducting and fast-diffusing network, providing the reported performance of the nanocomposite at high current rates.

To furtherly explore the high current performance of the nanocomposite, a galvanostatic cycling experiment for 250 cycles at $I_{spec} = 1000$ mAg^{-1} has been carried out and shown in Figure S6a.

First cycle coulombic efficiency is 50.09%, due to the aforementioned irreversible processes, which rapidly rises up to 99%. Specific Capacity values at the end of the experiment is 408 mAhg^{-1} with a capacity retention of 66.93%. Electrochemical features shown in Figure S6b and S6c are consistent with the already presented data, demonstrating a high long-term reversibility.

Another important contribution to the stability and performance of this nanocomposite material, is provided by the Polyacrylic acid binder, which thanks to its high number of carboxylic groups in the polymer backbone, enables the formation of hydrogen bonds with both copper oxide nanoparticles,improving the adhesion with the current collector[28,49,50] and the mechanical properties of the electrode. Moreover, as it has been already reported, the PAA binder acts

as artificial SEI,[30] which makes up for an additional stabilizing layer during electrochemical cycling. To assess the positive effect of the PAA binder on stability in galvanostatic cycling, a 300 cycles control experiment has been conducted using a PVdF based electrode, and compared with the PAA-based electrode, as can be seen in Figure S7, in which is apparent the improved stability and capacity retention of the latter.

To investigate the stability of the electrode-electrolyte interface over a high number of galvanostatic cycles, an Electrochemical Impedance Spectroscopy (EIS) experiment was done. In Figure 8 are shown the impedance spectra of selected cycles up to cycles 250.
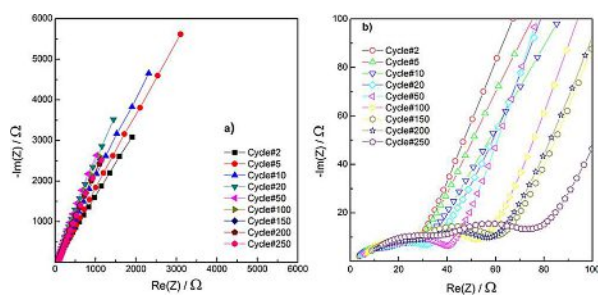
Figure 8. Electrochemical Impedance Spectroscopy: Nyquist Plots of selected cycles (a) overall view of the impedance spectra (b) detail on relevant features of the impedance spectra

In the insert of Figure 8 are visible the details of the high and medium frequency regions of the EIS spectra. In general, the spectra are characterized by a depressed high frequency semi-circle, due to the passivation layer, partially overlapped on a second depressed semi-circle at medium frequencies, due to the charge transfer processes. At low frequencies, diffusion processes are indicated by a sloping line, referred to as Warburg's impedance. The depression of the semicircles is generally due to inhomogeneities and porosity of the surface of the electrodes. The general tendency is a gradual impedance increase the with increasing cycle number, witnessing a certain long-term stability of the interface.

To better understand the evolution of the system, the spectra were subjected to a mathematical fitting procedure using the equivalent circuit method, by using Boukamp software.[51]

The chosen equivalent circuit, reported in Figure S8, in Boukamp's notation, is $R_{el}(R_{SEI}Q_{SEI})(R_{Ct}Q_{dl})Q_w$ where R_{el} is the electrical resistance associated with the electrolyte, $(R_{SEI}Q_{SEI})$ is a parallel between the resistance associated to the passivation layer (R_{SEI}) and its capacitance (Q_{SEI}), $(R_{Ct}Q_{dl})$ is a parallel between the electrical resistance associated with charge transfer processes (R_{Ct}) and the electrical double-layer capacitance (Q_{dl}), finally Q_w is the element associated with diffusion phenomena. The capacitive elements were treated as Constant Phase Elements (CPE).[52] In Figure S9 it is shown the evolution of the values of the fitted parameters: both R_{SEI} and the R_{Ct} tend to gradually increase with the number of cycles, which while on one hand testifies a certain stability of the interface, on the

other hand leads to a general deterioration over time, due to the probable mechanical degradation of the electrode due to the high number of cycles. In particular, the relatively low values of R_{Ct}, and their limited increase over the course of 250 cycles, is an indication of the good three-dimensional conductive network of the composite, which benefits, as previously explained, from a contiguity between the supporting carbon matrix, the crystalline nanodomains of metallic copper, and the active material itself.

Conclusions

In conclusion, electrospinning was employed to synthesize a novel $Cu_xO/Cu/C$ nanocomposite anode material for Li-ion batteries. The simplicity, flexibility and scalability of this approach allowed to obtain a robust fiber-like carbon architecture - with a sufficient porosity to enable good Li^+-ions diffusivity- in which Cu_2O nanoparticles are dispersed, but effectively confined. In addition, the dual step thermal annealing, provided a contiguous metallic Cu/Cu_2O structure, as testified by the TEM characterization, which ensured improved electronic conductivity. Electrochemical characterization evidenced voltammetric Cu_2O/CuO features consistent with literature data, and very good galvanostatic cycling performance with over 70% capacity retention after 450 cycles at 500 mAg^{-1} specific current, with specific capacity values over 500 mAhg^{-1} and coulombic efficiencies in the 99%+ range. High rate experiments data at several specific currents, and in a long cycling galvanostatic experiment at 1000 mAg^{-1} specific current also evidenced a high degree of stability. Electrochemical impedance spectroscopy was used to investigate the electrode-electrolyte interface in the long term, and the spectra were fitted using the equivalent circuit method. Resistance values show a slowly increasing trend, hint of a fairly stable interface and good retention of charge transfer kinetics. An additional contribution to the very good performance of this nanomaterial, is given by the PolyAcrylic Acid (PAA) and ethanol binder system, which can ensure easier and more sustainable electrode processing, better adhesion and improved electrode mechanical properties..

Experimental Section

The micro-nanofibers mats were prepared through an electrospinning process. The polymer blend was prepared dissolving Polyacrylonitrile (Mw=150000, Aldrich) in N,N-dimethylformamide (DMF, Aldrich). The solution was stirred for 20 h at 60 °C on a heating plate. CuO nanoparticles (Sigma-Aldrich) were then added, dispersed by sonication for 15 minutes in an ultrasonic bath (Elmasonic S30H) and stirred for 1 h at room temperature. The polymeric solution was electrospun at constant flow rate of 0.60 mlh^{-1} and with a DC voltage of 15–18 kV. Relative humidity and environmental temperature were 20% and 30 °C, respectively. The needle was placed at 15 cm distance from the plate collector (covered with an aluminum foil), at 10° of inclination angle. Electrospun mats were finally stabilized under air flow at 250 °C for 1 h at a heating rate of 5 °C min^{-1}. Thermal reduction was

performed at 700 °C under Ar:H$_2$ flow (95:5, 200 ml min^{-1}) at a heating rate of 10 °C min^{-1} to 400 °C and then 5 °C min^{-1} to 700 °C with a final plateau of 3 hours.

The crystalline phases present in the material were characterized by X-ray diffraction (XRD) using a Philips diffractometer (CuKα source, λ = 1.540 Å) in Bragg-Brentano θ/2θ geometry. Morphological characterization was conducted by means of Transmission Electron Microscopy (TEM, FEI Tecnai 200 kV cryo-TEM instrument) and Scanning Electron microscopy (ZEISS LEO 1550 SEM equipped with a X-MAXN EDX detector from Oxford Instruments). TEM pictures have been analyzed using the ImageJ software .[31] In particular simulated electron diffraction patterns have been reconstructed by performing a Fast-Fourier Transform (FFT) analysis of selected areas of the micrographs using the routines embedded in the ImageJ code. For the handling of the SEM samples, the Cu$_x$O–C pristine powder and fresh electrodes were not subjected to any special treatment before analysis. Thermogravimetric measurements were carried out on a Netzsch One TGA instrument in the temperature range 25 °C–950 °C at a heating rate of 10 °C min^{-1}. Raman and FTIR measurements were recorded on a Horiba iHR320 spectrometer using a 633 nm laser as a light source and a Perkin-Elmer Spectrum TWO instrument, respectively.

Electrode slurries have been prepared mixing Cu$_x$O–C powders as active material, SuperP (Timcal Ltd.) as conductive agent, and Poly (Acrylic Acid) (PAA, Sigma Aldrich, Mw ~450,000) dissolved in ethanol as polymeric binder, using a 80 (Active Material) : 10 (Conductive Agent): 10 (Binder) mass ratio. The slurry has been stirred overnight, spread onto a 10 μm copper foil using the "Doctor Blade" technique with a wet thickness of 150 μm and dried 2 h at T = 50 °C on a heating plate. The electrode foil has been calendared and 9 mm-diameter circular electrodes have been cut and dried at 120 °C under vacuum for 12 h. Active material mass loading was about ≈1 mg cm^{-2}.

Three-electrode T-shaped cells have been assembled in Ar-filled glove box (O$_2$ < 0.1 ppm–H$_2$O < 0.1 ppm), using metal lithium (Sigma-Aldrich) as counter and reference electrodes, and 12 mm glass fiber disks (Whatman GF/A) as separators. A volume of 300 μl of a LiPF$_6$ 1 M solution in ethylene carbonate:dimethyl carbonate (EC:DMC) 1:1 v/v (Solvionic, France) has been used as electrolyte. Each cell has been subjected to 12 h period of open circuit voltage (OCV), in order to enable full wetting of separator and electrolyte. Electrochemical characterization has been performed using a VMP-2Z multi-channel galvanostat-potentiostat (Bio-Logic, France) in the 0.005 V < E < 3.000 V potential range, at specific currents ranging from 100 mA g^{-1} to 10000 mA g^{-1}. Electrochemical impedance spectroscopy (EIS) has been performed in the 100 kHz–10 mHz frequency range, by applying a bias potential of E = 3.0 V and a sinusoidal amplitude ΔE = ±5 mV. All potential values are given vs. Li$^+$/Li. Specific capacity values have been calculated on the basis of the electrode Active Material weight. All electrochemical measurements have been recorded in a Tenney TPS-TJR environmental chamber at T = 20 ± 0.1 °C room temperature.

Acknowledgements

Conflict of interest

The authors declare no conflict of interest.

[1] G. E. Blomgren, *J. Electrochem. Soc.* **2017**, *164*, A5019.
[2] M. N. Obrovac, V. L. Chevrier, *Chem. Rev.* **2014**, *114*, 11444.
[3] A. Kraytsberg, Y. Ein-Eli, *J. Solid State Electrochem.* **2017**, 1.
[4] L. Zhang, H. Bin Wu, X. W. Lou, *Adv. Energy Mater.* **2014**, *4*, 1.
[5] D. Bresser, F. Mueller, M. Fiedler, S. Krueger, R. Kloepsch, D. Baither, M. Winter, E. Paillard, S. Passerini, *Chem. Mater.* **2013**, *25*, 4977.
[6] S. H. Yu, S. H. Lee, D. J. Lee, Y. E. Sung, T. Hyeon, *Small* **2016**, *12*, 2146.
[7] G. Carbonari, F. Maroni, M. Pasqualini, R. Tossici, F. Nobili, *Electrochim. Acta* **2017**, *247*, DOI 10.1016/j.electacta.2017.06.148.
[8] B. Das, M. V. Reddy, P. Malar, T. Osipowicz, G. V. Subba Rao, B. V. R. R. Chowdari, *Solid State Ionics* **2009**, *180*, 1061.
[9] B. Wu, H. Song, J. Zhou, X. Chen, *Chem. Commun.* **2011**, *47*, 8653.
[10] H. Li, G. Richter, J. Maier, *Adv. Mater.* **2003**, *15*, 736.
[11] D. Bresser, E. Paillard, P. Niehoff, S. Krueger, F. Mueller, M. Winter, S. Passerini, *ChemPhysChem* **2014**, *15*, 2177.
[12] J. R. Szczech, S. Jin, *Energy Environ. Sci.* **2011**, *4*, 56.
[13] C. Wang, D. Fang, H. Wang, Y. Cao, W. Xu, X. Liu, Z. Luo, G. Li, M. Jiang, C. Xiong, *Sci. Rep.* **2016**, *6*, 20826.
[14] G. Li, M. Jing, Z. Chen, B. He, M. Zhou, Z. Hou, *RSC Adv.* **2017**, *7*, 10376.
[15] S. Xie, D. Cao, Y. She, H. Wang, J.-W. Shi, M. K. H. Leung, C. Niu, *Chem. Commun.* **2018**, *1*, 2.
[16] P. Adelhelm, Y.-S. Hu, M. Antonietti, J. Maier, B. M. Smarsly, *J. Mater. Chem.* **2009**, *19*, 1616.
[17] Z. Wang, D. Luan, S. Madhavi, Y. Hu, X. W. (David) Lou, *Energy Environ. Sci.* **2012**, *5*, 5252.
[18] L. Wang, Y. Yu, P. C. Chen, D. W. Zhang, C. H. Chen, *J. Power Sources* **2008**, *183*, 717.
[19] J. O. Besenhard, M. Winter, J. Yang, W. Biberacher, *J. Power Sources* **1995**, *54*, 228.
[20] K. Evanoff, A. Magasinski, J. Yang, G. Yushin, *Adv. Energy Mater.* **2011**, *1*, 495.
[21] P. Lian, X. Zhu, H. Xiang, Z. Li, W. Yang, H. Wang, *Electrochim. Acta* **2010**, *56*, 834.
[22] C. Fu, C. Song, L. Liu, W. Zhao, *X. Xie* **2016**, *11*, 154.
[23] A. Birrozzi, R. Raccichini, F. Nobili, M. Marinaro, R. Tossici, R. Marassi, *Electrochim. Acta* **2014**, *137*, 228.
[24] M. MacÍas, A. Chacko, J. P. Ferraris, K. J. Balkus, *Microporous Mesoporous Mater.* **2005**, *86*, 1.
[25] P. F. Teh, S. S. Pramana, Y. Sharma, Y. W. Ko, S. Madhavi, *ACS Appl. Mater. Interfaces* **2013**, *5*, 5461.
[26] M. Agostini, J.-Y. Hwang, H. M. Kim, P. Bruni, S. Brutti, F. Croce, A. Matic, Y.-K. Sun, *Adv. Energy Mater.* **2018**, *8*, 1803205.
[27] F. Wang, J. Cai, J. Yu, C. Li, Z. Yang, *ChemElectroChem* **2018**, *5*, 51.
[28] F. Wang, P. Zhu, J. Pan, C. Li, Z. Yang, *RSC Adv.* **2017**, *7*, 48294.
[29] S. Zeng, R. Zhao, A. Li, S. Xue, D. Lv, Q. Luo, D. Shu, H. Chen, *Appl. Surf. Sci.* **2019**, *463*, 211.
[30] D. E. Yoon, C. Hwang, N. R. Kang, U. Lee, D. Ahn, J. Y. Kim, H. K. Song, *ACS Appl. Mater. Interfaces* **2016**, *8*, 4042.
[31] A. Magasinski, B. Zdyrko, I. Kovalenko, B. Hertzberg, R. Burtovyy, C. F. Huebner, T. F. Fuller, I. Luzinov, G. Yushin, *ACS Appl. Mater. Interfaces* **2010**, *2*, 3004.
[32] S. Komaba, K. Shimomura, N. Yabuuchi, T. Ozeki, H. Yui, K. Konno, *J. Phys. Chem. C* **2011**, *115*, 13487.
[33] S. Komaba, N. Yabuuchi, T. Ozeki, Z. J. Han, K. Shimomura, H. Yui, Y. Katayama, T. Miura, *J. Phys. Chem. C* **2012**, *116*, 1380.
[34] Z. M. Huang, Y. Z. Zhang, M. Kotaki, S. Ramakrishna, *Compos. Sci. Technol.* **2003**, *63*, 2223.
[35] J. Xue, J. Xie, W. Liu, Y. Xia, *Acc. Chem. Res.* **2017**, *50*, 1976.
[36] T. H. Hwang, Y. M. Lee, B. S. Kong, J. Seo, J. W. Choi, n.d., 1.
[37] I. M. Alarifi, W. S. Khan, R. Asmatulu, *PLoS One* **2018**, *13*, 1.
[38] I. Gergin, E. Ismar, A. S. Sarac, *Beilstein J. Nanotechnol.* **2017**, *8*, 1616.
[39] Y. P. Wu, E. Rahm, R. Holze, *J. Power Sources* **2003**, *114*, 228.
[40] C. S. Sharma, H. Katepalli, A. Sharma, M. Madou, *Carbon N. Y.* **2011**, *49*, 1727.
[41] A. Kirfel, K. Eichhorn, *Acta Crystallogr. Sect. A Found. Crystallogr.* **1990**, *46*, 271.
[42] J. Donohue, *The Structure of Elements*, Wiley, New York (US), **1974**.
[43] E. Peled, S. Menkin, *J. Electrochem. Soc.* **2017**, *164*, A1703.
[44] M. Nie, B. L. Lucht, *J. Electrochem. Soc.* **2014**, *161*, A1001.

[45] S. J. Rezvani, F. Nobili, R. Gunnella, M. Ali, R. Tossici, S. Passerini, A. Di Cicco, *J. Phys. Chem. C* **2017**, *121*, 26379.

[46] H. Liu, Y. Lin, Z. Hu, R. Hu, H. Ruan, *L. Zhang* **2016**, *2016*, 2.

[47] C. Wang, Q. Li, F. Wang, G. Xia, R. Liu, D. Li, N. Li, J. S. Spendelow, G. Wu, *ACS Appl. Mater. Interfaces* **2014**, *6*, 1243.

[48] J. Li, C. Wu, L. Guan, *Test* **2010**, 18431.

[49] J. R. Dahn, T. Zheng, Y. Liu, J. S. Xue, *Science* **1995**, *270*, 590.

[50] J. R. Dahn, T. Zheng, Y. Liu, J. S. Xue, *Science* **1995**, *270*, 590.

[51] B. A. Boukamp, *Solid State Ionics* **1986**, *20*, 31.

[52] D. J. R. M. E. Barsoukov, *Impedance Spectroscopy*, John Wiley & Sons, Inc., Hoboken, NJ, USA, **2005**.